

High-resolution wide-field magnetic imaging with sparse sampling using nitrogen-vacancy centers

Keqing Liu^{1,2,3}, Jiazhao Tian^{1,2,3,*}, Bokun Duan^{1,2,3}, Hao Zhang^{1,2,3}, Kangze Li^{1,2,3}, Guofeng Zhang⁴, Fedor Jelezko⁵, Ressa S. Said⁵, Jianming Cai^{6,7}, and Liantuan Xiao^{1,2,3,4,*}

¹College of Physics and Optoelectronic Engineering, Taiyuan University of Technology, Taiyuan 430000, People's Republic of China

²Shanxi Key Laboratory of Precision Measurement Physics, Taiyuan University of Technology, Taiyuan 030024, China

³Key Laboratory of Advanced Transducers and Intelligent Control System, Ministry of Education, and Shanxi Province, Taiyuan University of Technology, Taiyuan 030024, China

⁴State Key Laboratory of Quantum Optics Technologies and Devices, Institute of Laser Spectroscopy, Collaborative Innovation Center of Extreme Optics, Shanxi University, Taiyuan, 030006, China

⁵Institute for Quantum Optics & Center for Integrated Quantum Science and Technology, Universität Ulm, 89081 Ulm, Germany

⁶School of Physics, Hubei Key Laboratory of Gravitation and Quantum Physics, Institute for Quantum Science and Engineering, International Joint Laboratory on Quantum Sensing and Quantum Metrology, Center for Intelligence and Quantum Science (CIQS), Huazhong University of Science and Technology, Wuhan 430074, China

⁷Wuhan Institute of Quantum Technology, Wuhan 430074, China

February 3, 2026

**tianjiazhao@tyut.edu.cn, *xlt@sxu.edu.cn*

Abstract

Nitrogen–vacancy (NV) centers in diamond enable quantitative magnetic imaging, yet practical implementations must balance spatial resolution against acquisition time (and thus per-pixel sensitivity). Single-NV scanning magnetometry achieves genuine nanoscale resolution, nonetheless requires typically a slow pixel-by-pixel acquisition. Meanwhile, wide-field NV-ensemble microscopy provides parallel readout over a large field of view, however is jointly limited by the optical diffraction limit and the sensor–sample standoff. Here, we present a sparse-sampling strategy for reconstructing high-resolution wide-field images from only a small number of measurements. Using simulated NV-ensemble detection of ac magnetic fields, we show that a mean-adjusted Bayesian estimation (MABE) framework can reconstruct 10^4 -pixel images from only 25 sampling points, achieving SSIM values exceeding 0.999 for representative smooth field distributions, while optimized dynamical-decoupling pulse sequences yield an approximately twofold improvement in magnetic-field sensitivity. The method further clarifies how sampling patterns and sampling density affect reconstruction accuracy and suggests a route toward faster and more scalable magnetic-imaging architectures that may extend to point-scanning NV sensors and other magnetometry platforms, such as SQUIDs, Hall probes, and magnetic tunnel junctions.

1 Introduction

Nitrogen–vacancy (NV) centers in diamond provide a well-defined electronic spin system in a chemically robust solid-state host and have therefore become a central platform for quantum sensing and metrology [1],

[2, 3]. In these centers, the ground-state spin sublevels shift in response to external perturbations and can be read out optically, enabling quantitative measurements of magnetic fields via shifts of the spin resonance frequencies detected by optically detected magnetic resonance (ODMR) [4], electric fields through Stark shifts [5], microwave-frequency magnetic fields via driven spin transitions [6], as well as temperature through the temperature dependence of the zero-field splitting parameter [7, 8, 2], and lattice strain via strain-induced shifts and splittings of the NV spin levels [2, 9, 10], by means of optically detected magnetic resonance techniques. Within this general framework, NV-based magnetometry has emerged as one of the most mature sensing modalities, with applications ranging from nanoscale studies of condensed-matter systems [11] and imaging of geological and mineral samples using quantum-diamond microscopy [12], to biological signal detection and biomedical contexts [13], as well as diagnosis and fingerprinting of activity in integrated circuits [14, 15].

For spatially resolved measurements, magnetic-field imaging places simultaneous demands on spatial resolution and on the acquisition time required to reach a target field sensitivity per pixel, reflecting the standard $1/\sqrt{T}$ scaling of sensitivity with averaging time in NV magnetometry [16, 17]. Scanning-probe approaches based on single, shallow NV centers attached to atomic-force or planar probes can achieve genuine nanoscale spatial resolution by maintaining sensor-sample separations of only a few tens of nanometres, thereby accessing the near-field stray-field distribution of the sample [18, 19, 20]. In practice, however, each pixel typically requires dwell times on the order of milliseconds or longer to obtain sufficient signal-to-noise ratio, so that high-resolution images are restricted to fields of view of at most a few to a few tens of square micrometres and acquisition times of minutes or more [18, 19, 12].

An alternative architecture employs near-surface NV ensembles interrogated in a widefield optical microscope, where NV fluorescence is detected on a camera to form spatially resolved maps of local magnetic fields in parallel across the full diamond area [12, 17]. Such quantum diamond microscopes typically offer fields of view ranging from tens of micrometres up to the millimetre scale while retaining quantitative magnetometric performance and mitigating artefacts associated with mechanical drift of scanning probes [12, 15]. Because the four crystallographic NV orientations can be addressed separately, ensemble-based widefield platforms also enable vector reconstruction of the local magnetic field and support measurements at or near zero bias field [17, 21, 22, 23].

A key limitation of conventional widefield NV microscopy is that the lateral spatial resolution is jointly determined by the sensor-sample standoff and the diffraction limit of far-field imaging optics, such that even with high-numerical-aperture objectives the effective resolution typically remains in the few-hundred-nanometre range [12, 17]. To relax this constraint, several super-resolution strategies have been adapted to NV centers, including stimulated-emission-depletion microscopy of single NVs in bulk diamond and nanodiamonds [24, 25], charge-state-depletion schemes based on nonlinear control of NV^-/NV^0 charge conversion [26], and more recently super-resolution-enabled widefield quantum-diamond microscopy using structured illumination [27]. These techniques can push the effective spatial resolution into the $\sim 10\text{--}100\text{ nm}$ regime, but most implementations still rely on scanning or repeated patterned excitation and therefore do not yet offer the acquisition speed and simplicity of conventional widefield NV microscopy [17, 26, 27].

In this work, we propose a sparse-sampling strategy that enables high-resolution widefield imaging from a limited number of measurement points. Using simulated NV ensemble measurements of ac magnetic fields as an illustrative example, we demonstrate that by sampling only 25 points within the field of view and applying a mean-adjusted Bayesian estimation (MABE) scheme [28, 29, 30, 31, 32, 33], a high-resolution image containing 10^4 pixels can be reconstructed. For magnetic-field patterns comprising different numbers of extrema, the reconstructed images achieve structural similarity index (SSIM) values exceeding 0.999. Moreover, by optimizing the dynamical-decoupling pulse sequence, the magnetometry contrast is enhanced, leading to an approximate twofold improvement in magnetic-field sensitivity. We further analyze how sampling strategies and sampling density affect reconstruction quality, providing guidance for adapting the method to different application requirements.

As a general sparse-sampling imaging framework, the proposed MABE approach can be straightforwardly extended to point-scanning magnetometry platforms, including single-NV-based schemes as

well as other sensor technologies such as superconducting quantum interference devices (SQUIDs), Hall sensors, and magnetic tunnel junctions. These results point toward fast, compact, and scalable quantum magnetic imaging architectures with potential applications in on-chip magnetic diagnostics, real-time field mapping, and integrated quantum metrology [28, 29, 30, 31, 32, 33].

2 AC Magnetic Field Measurement

The negatively charged nitrogen-vacancy (NV^-) center in diamond possesses an electron spin $S = 1$ ground state with a zero-field splitting $D = 2\pi \times 2.88 \text{ GHz}$ [34]. When driven by a sequence of microwave pulses that flip the spin state at each zero crossing of an ac magnetic field, the field amplitude can be extracted from the accumulated spin phase. We consider a two-level subspace spanned by $|0\rangle$ and $|1\rangle$ (representing $|+1\rangle$ or $| -1\rangle$) and denote the actual frequency of microwave as ω . In the interaction picture with respect to $\omega\sigma_z$, the Hamiltonian is

$$H = \frac{\delta_0}{2}\sigma_z + H_{\text{AC}} + H_{\text{C}}, \quad (1)$$

where δ_0 is the detuning between the microwave frequency and the $|0\rangle \leftrightarrow |1\rangle$ transition, $H_{\text{AC}} = g_{\text{AC}} \cos(\omega_{\text{AC}}t)\sigma_z$ describes the ac magnetic field, and $H_{\text{C}} = \Omega_x(t)\sigma_x + \Omega_y(t)\sigma_y$ represents the microwave control pulses.

In the ideal noiseless case, π pulses are applied at each zero crossing of the ac field, corresponding to a modulation function $f(t) = \text{sgn}[\sin(\omega_{\text{AC}}t)]$. The accumulated relative phase is [1, 35, 36]

$$\Phi(t) = 2 \int_0^t g_{\text{AC}} \cos(\omega_{\text{AC}}t') f(t') dt' \approx \frac{4}{\pi} g_{\text{AC}} t. \quad (2)$$

After a Ramsey measurement, the population of $|0\rangle$ follows $P_0 = \frac{1}{2}[1 + \cos\Phi(t)]$. The magnetic-field amplitude is given by $B = g_{\text{AC}}/\gamma = \pi\omega/(4\gamma)$, where γ is the gyromagnetic ratio of the NV center.

In practical NV ensemble measurements, inhomogeneous broadening induced by nonuniform local environments reduces the fidelity of π pulses, thereby degrading the spin-population contrast and ultimately the magnetic-field sensitivity. We decompose the detuning term as $\delta_0 = \delta + \delta_d(t)$, where δ represents time-independent inhomogeneous broadening described by a Gaussian distribution [37]

$$p(\delta) = \frac{1}{\sqrt{2\pi}\sigma_g} \exp\left(-\frac{\delta^2}{2\sigma_g^2}\right), \quad (3)$$

and $\delta_d(t)$ denotes time-dependent noise following an Ornstein–Uhlenbeck process [38, 39]

$$\delta_d(t + \Delta t) = \delta_d(t)e^{-\Delta t/\tau} + \left[\frac{c\tau}{2}\left(1 - e^{-2\Delta t/\tau}\right)\right]^{1/2} n_\delta, \quad (4)$$

where τ and c are the correlation time and diffusion constant, respectively, and $n_\delta \sim \mathcal{N}(0, 1)$. We set the full width at half maximum (FWHM) of the static detuning distribution to $W = 2\sqrt{2\ln 2}\sigma_g = 2\pi \times 26.5 \text{ MHz}$, the correlation time to $\tau = 20 \mu\text{s}$, and the diffusion coefficient to $\sqrt{c\tau/2} = 2\pi \times 50 \text{ kHz}$ [35]. The pulse duration is fixed at $T_{\text{pulse}} = 50 \text{ ns}$, corresponding to a Rabi frequency of 10 MHz, with an interpulse interval $\tau_p = 950 \text{ ns}$ and a total evolution time $t = 8N(T_{\text{pulse}} + \tau_p) = 400 \mu\text{s}$ where the sequence number $N = 50$.

Under these noise conditions, the spin-population evolution obtained using an XY-8 sequence with rectangular π pulses is shown in Fig. 1(c) (blue curve with dot markers), where a pronounced reduction in contrast to below 0.2 is observed.

To mitigate this effect, we employ a phase-modulated (PM) pulse optimization strategy [40] to enhance pulse fidelity and thereby improve population contrast and magnetic-field sensitivity. The PM control Hamiltonian is expressed as

$$H_{\text{PM}}(t) = \sum_{j=1}^N \frac{a_j}{2} \left\{ \cos\left[\frac{b_j}{\nu_j} \sin(\nu_j t)\right] \sigma_x + \sin\left[\frac{b_j}{\nu_j} \sin(\nu_j t)\right] \sigma_y \right\}, \quad (5)$$

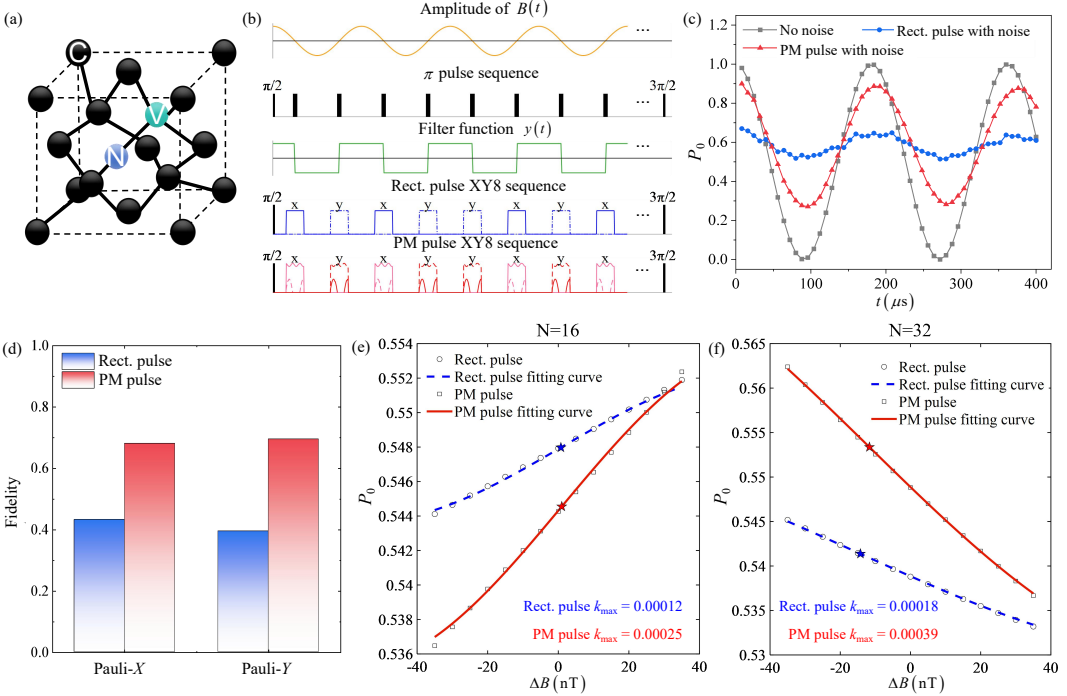


Figure 1: (a) Schematic illustration of an NV center in the diamond lattice. (b) Schematic representation of the temporal correspondence among the target AC magnetic field, the control pulses, and the filter function. From top to bottom: amplitude of the target AC magnetic field; ideal infinite-duration pulse sequence applied at the zero crossings; the corresponding filter function for the ideal pulse sequence; XY-8 rectangular-pulse sequence with finite pulse width; and XY-8-PM sequence with finite pulse width. In our simulation, we set the pulse duration $T_{\text{pulse}} = 50$ ns, the pulse interval $\tau_p = 950$ ns, and the total evolution time $t = 8N (T_{\text{pulse}} + \tau_p) = 400$ μ s, with the sequence number $N = 50$. (c) Time evolution of the NV spin population. The gray line with square markers corresponds to the noiseless case using ideal infinite pulses, whereas the blue line with dot markers and the red line with triangular markers correspond to rectangular pulses and PM pulses, respectively, in the presence of inhomogeneous broadening noise and the dynamical noise (see the main text). (d) Comparison of the Pauli-X and Pauli-Y gate fidelities for rectangular pulses and PM pulses, with fidelity defined in Eq. (7) and PM pulse forms given in Eqs. (8)–(9). (e) Dependence of the normalized spin population for $N = 16$ ($t = 128$ μ s). The starred markers denote the points of maximum slope: $k = 0.00012$ for rectangular pulses and $k = 0.00025$ for PM pulses. (d) Dependence of the normalized spin population for $N = 32$ ($t = 256$ μ s). The starred markers denote the points of maximum slope: $k = 0.00018$ for rectangular pulses and $k = 0.00039$ for PM pulses.

which generates a multifrequency waveform with a reduced parameter space. The parameters $\{a_j, b_j, \nu_j\}$ are optimized by maximizing the objective function

$$F_{\text{obj}}^G = \mathcal{N} \sum_{k=1}^M p(\delta_k) f_g(\delta_k), \quad (6)$$

where $\mathcal{N} = [\sum_k p(\delta_k)]^{-1}$ is a normalization factor and

$$f_g(\delta) = \frac{1}{2} + \frac{1}{3} \sum_{\kappa=x,y,z} \text{Tr} \left(U_{\text{tar}} \frac{\sigma_\kappa}{2} U_{\text{tar}}^\dagger U_\delta \frac{\sigma_\kappa}{2} U_\delta^\dagger \right) \quad (7)$$

is the average gate fidelity [41, 42]. Here $U_\delta = T \exp[-i \int_0^t H(\delta, t') dt']$ and the target operators U_{tar} correspond to Pauli-X and Pauli-Y gates for π_x and π_y pulses, respectively.

We uniformly sample $M = 15$ detuning values within the interval $[-W, W]$, covering approximately 98% of the distribution. The pulse amplitude is constrained below $2\pi \times 10$ MHz. The optimization can be carried out using standard implementations of direct-search optimization methods.

The resulting improvements in Pauli-X and Pauli-Y gate fidelities are shown in Fig. 1(d), where both increase from approximately 0.43 to 0.68. To preserve orthogonality between π_x and π_y pulses in the XY-8 sequence, identical PM parameters are used. We adopt the parameter set $a = 0.0628$, $b = 0.0830$, and $\nu = 0.0316$, yielding the control Hamiltonians

$$H_{\pi_x}(t) = \frac{a}{2} \left[\cos \left(\frac{b}{\nu} \sin \nu t \right) \sigma_x + \sin \left(\frac{b}{\nu} \sin \nu t \right) \sigma_y \right], \quad (8)$$

and

$$H_{\pi_y}(t) = \frac{a}{2} \left[\cos \left(\frac{b}{\nu} \sin \nu t \right) \sigma_y - \sin \left(\frac{b}{\nu} \sin \nu t \right) \sigma_x \right]. \quad (9)$$

As shown in Fig. 1(c), the optimized XY-8 sequence employing PM pulses enhances the population contrast to approximately 0.6 in the presence of noise, representing a threefold improvement over the unoptimized case. This contrast enhancement directly translates into improved magnetic-field sensitivity [43, 35]

$$\eta = \frac{\sigma}{(\partial P / \partial B)} \sqrt{T}, \quad (10)$$

where σ is the standard deviation of single-shot readout noise which typically arises from the photon shot noise, $\partial P / \partial B$ is the maximum slope of the population response to magnetic-field amplitude, and T is the measurement duration. Evaluating $\partial P / \partial B$ at $N = 16$ and $N = 32$, corresponding to evolution times $t = 128 \mu\text{s}$ and $256 \mu\text{s}$, yields more than a twofold increase in slope (Fig. 1(e,f)), leading to sensitivity improvements from $0.94 \text{ nT}/\sqrt{\text{Hz}}$ to $0.45 \text{ nT}/\sqrt{\text{Hz}}$ and from $1.33 \text{ nT}/\sqrt{\text{Hz}}$ to $0.64 \text{ nT}/\sqrt{\text{Hz}}$, respectively, where σ was taken to be 10^{-2} [43].

3 Imaging with the MABE Method

In this section, we introduce the mean-adjusted Bayesian estimation (MABE) method that enables rapid imaging of the magnetic field distribution. High-resolution magnetic field imaging typically relies on dense point-by-point scanning, which is highly time-consuming. In contrast, Bayesian-based estimation methods [44] allow the full distribution to be inferred from only a small number of samples. We denote \mathbf{x} as the two-dimensional coordinate, $y(\mathbf{x})$ as the measured magnetic field value at \mathbf{x} , $\hat{y}(\mathbf{x})$ as the predicted magnetic field value, and \mathbf{s} as the coordinates of the actual measurement samples. The correlation between the errors at two coordinates \mathbf{x}_i and \mathbf{x}_j is defined as $\text{Corr} [\epsilon(\mathbf{x}_i), \epsilon(\mathbf{x}_j)] = \exp [-d(\mathbf{x}_i, \mathbf{x}_j)]$ [45], where d is the distance function whose specific form is to be determined. The best linear unbiased predictor for $y(\mathbf{x})$ can be expressed as [46]

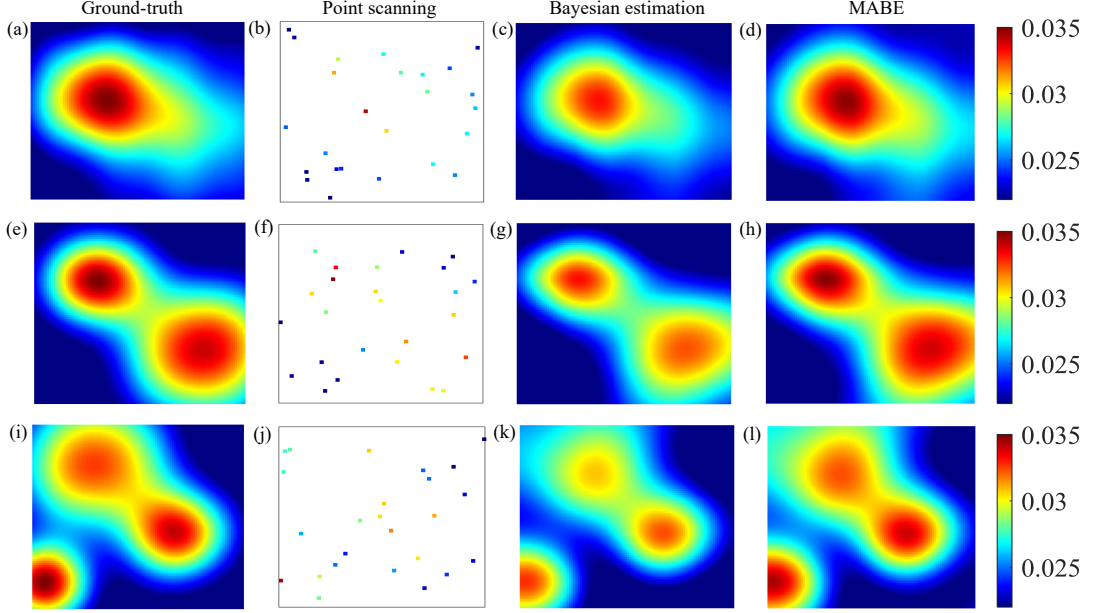


Figure 2: Imaging performance for magnetic-field distributions with different numbers of extrema. (a),(e),(i) Simulated ground-truth magnetic-field maps containing single, two, and three extrema. (b),(f),(j) Measurement results at 25 randomly distributed sampling points (marker size enlarged for clarity). (c),(g),(k) Magnetic-field maps reconstructed directly from the sampled data using Bayesian estimation method, yielding 10^4 -pixel images. (d),(h),(l) Magnetic-field maps reconstructed from the same sampled data using the MABE method, also producing 10^4 -pixel images.

$$\hat{y}(\mathbf{x}) = \hat{\mu} + \mathbf{r}'(\mathbf{x}) \mathbf{R}^{-1} (\mathbf{y}(\mathbf{s}) - \hat{I}\hat{\mu}), \quad (11)$$

where \mathbf{R} is an $n \times n$ correlation matrix with elements $\text{Corr}[\epsilon(\mathbf{s}_i), \epsilon(\mathbf{s}_j)]$, $\mathbf{r}(\mathbf{x}) = [R(\mathbf{s}_1, \mathbf{x}), \dots, R(\mathbf{s}_n, \mathbf{x})]'$ is an $n \times 1$ vector representing the correlation between the errors of the sampling points and the untested input \mathbf{x} , with $R(\mathbf{s}_i, \mathbf{x}) = \text{Corr}[\epsilon(\mathbf{s}_i), \epsilon(\mathbf{x})]$, $\hat{\mu} = (\hat{I}' \mathbf{R}^{-1} \hat{I})^{-1} \hat{I}' \mathbf{R}^{-1} \mathbf{y}(\mathbf{s})$, and \hat{I} is the $n \times 1$ vector with all elements equal to 1. We take the distance function in the form $d(\mathbf{s}_i, \mathbf{s}_j) = \sum_{h=1}^2 \alpha_h |s_{i,h} - s_{j,h}|^{P_h}$, with $\alpha_h \geq 0$ and $P_h \in [1, 2]$, where the parameters α_h and P_h are optimized by maximizing the likelihood function of the samples described by [46]

$$\frac{1}{(2\pi)^{n/2} (\sigma^2)^{n/2} |\mathbf{R}|^{1/2}} \exp \left[-\frac{(\mathbf{y}(\mathbf{s}) - \hat{I}\hat{\mu})' \mathbf{R}^{-1} (\mathbf{y}(\mathbf{s}) - \hat{I}\hat{\mu})}{2\sigma^2} \right], \quad (12)$$

where $|\mathbf{R}|$ denotes the determinant of \mathbf{R} . Through this procedure, a high-resolution magnetic field map can be predicted by measuring the fields at only n sample locations.

We validate the method using three simulated magnetic-field distributions with single, two, and three extrema, shown in Fig. 2(a,e,i). Measurements at each sampling point employ the sensitivity-enhanced PM-pulse protocol described above. Sampling locations are generated by perturbing uniformly spaced grid points with uniformly distributed displacements bounded to 30% of the field-of-view size. With $n = 25$, direct point-wise interpolation captures only coarse features (Fig. 2(b,f,j)), whereas Bayesian estimation reconstructs a 100×100 pixel map in good agreement with the ground truth (Fig. 2(c,g,k)).

Due to measurement errors at individual sampling points, the reconstructed global distribution can exhibit a residual systematic deviation from the ground truth. To mitigate this bias and improve the overall accuracy, we introduce a reference-based mean-adjustment procedure, which yields the improved reconstructions shown in Fig. 2(d,h,l). Specifically, ten reference points \mathbf{r} with nominal values $y_{\text{nom}}(\mathbf{r})$ were selected to be uniformly distributed so as to span the value range covered by the 25 sampling-point

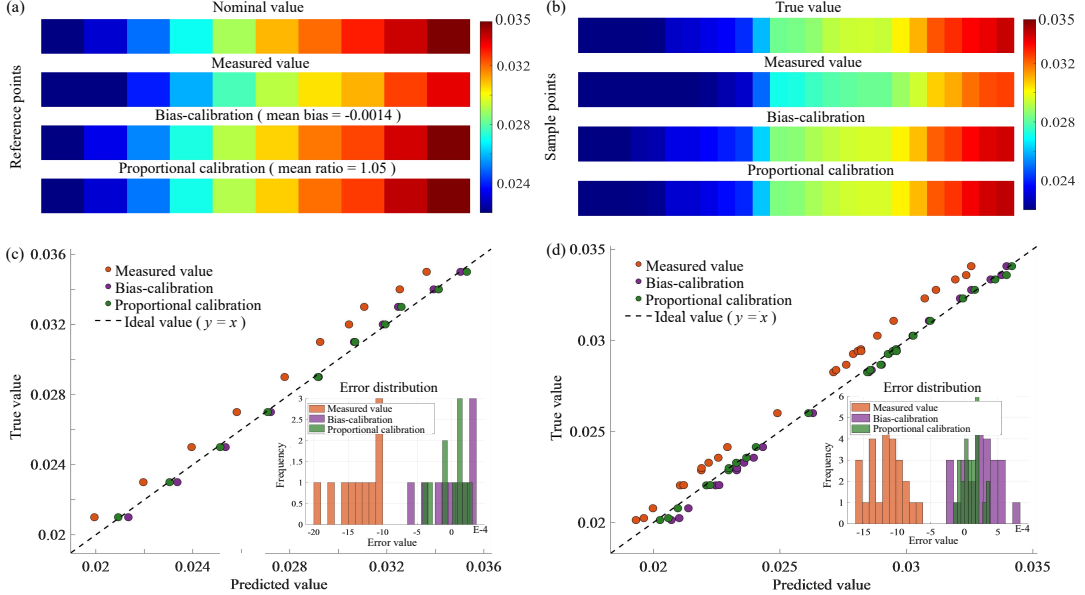


Figure 3: Illustration of the reference-based mean-adjustment procedure. (a) Values at the reference points, shown as nominal values, measured values, bias-calibrated values, and proportionally calibrated values. The reference values are uniformly chosen so as to span the range covered by the 25 sampling-point measurements. (b) Ground-truth values, unadjusted measurements, bias-calibrated values, and proportionally calibrated values for the 25 sampling points, where the calibration coefficients are obtained from the reference points. (c) Error comparison for the reference points before calibration, after bias calibration, and after proportional calibration. (d) Error comparison for the sampling points before calibration, after bias calibration, and after proportional calibration. For both the reference and sampling points, proportional calibration produces error distributions that are more tightly centered around zero than bias calibration.

measurements. These reference points were measured using the same protocol under identical noise conditions. The top two rows of Fig. 3(a) show the nominal and measured values at the reference points. The deviations between the measured and nominal reference values are then used to calibrate the measured data employed for image reconstruction.

We denote the mean of the nominal and measured reference values by $\overline{y_{\text{nom}}(\mathbf{r})}$ and $\overline{y(\mathbf{r})}$, respectively, and define the adjusted value at coordinate \mathbf{x} as $y_{\text{ad}}(\mathbf{x})$. We consider two calibration schemes. The bias-calibration approach applies an additive correction,

$$y_{\text{ad}}(\mathbf{x}) = y(\mathbf{x}) + \left(\overline{y_{\text{nom}}(\mathbf{r})} - \overline{y(\mathbf{r})} \right), \quad (13)$$

whereas the proportional calibration rescales the data multiplicatively,

$$y_{\text{ad}}(\mathbf{x}) = y(\mathbf{x}) \frac{\overline{y_{\text{nom}}(\mathbf{r})}}{\overline{y(\mathbf{r})}}. \quad (14)$$

The resulting calibrated reference values for both schemes are shown in the bottom two rows of Fig. 3(a). Compared with bias calibration, proportional calibration yields smaller absolute errors and a narrower error spread for the reference points, as shown in Fig. 3(c). Fig. 3(b) summarizes, for the 25 sampling points, the ground-truth values, the unadjusted measurements, and the values obtained after bias and proportional calibration; the corresponding errors are shown in Fig. 3(d). These results verify the effectiveness of proportional calibration. Consequently, we adopt proportional calibration according to Equation (14) to generate the adjusted values used for the MABE reconstructions in Fig. 2(d,h,l).

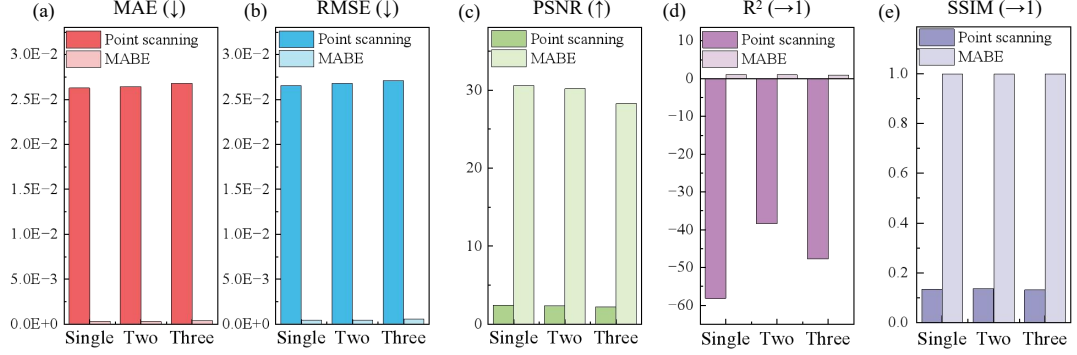


Figure 4: Quantitative image-quality metrics for the MABE reconstruction under irregular magnetic-field distributions containing single, two, and three extrema, as the sampling number n varies: (a) mean absolute error (MAE); (b) root mean square error (RMSE); (c) peak signal-to-noise ratio (PSNR); (d) coefficient of determination (R^2); (e) structural similarity index (SSIM). In the figure captions, the arrows shown after each metric indicate whether smaller values (↓), larger values (↑), or values closer to unity (→ 1) correspond to better reconstruction performance.

Fig. 4 quantitatively demonstrates the performance gain of the MABE method for the three magnetic-field distributions shown in the first column of Fig. 2, using five evaluation metrics [47, 48]: mean absolute error (MAE), which measures the average absolute deviation; peak signal-to-noise ratio (PSNR), which characterizes reconstruction fidelity relative to noise; root mean square error (RMSE), which weights larger errors more strongly; coefficient of determination (R^2), which summarizes goodness of fit; and structural similarity index measure (SSIM), which evaluates structural similarity. In general, smaller MAE and RMSE, together with larger PSNR and values of R^2 and SSIM closer to unity, indicate better reconstruction quality. Negative values of R^2 may occur when the reconstruction fits the data worse than the trivial predictor given by a horizontal line at the mean of the observed data [49, 50].

For magnetic-field distributions containing single, two, and three extrema, the proposed MABE approach yields substantial improvements compared with images obtained directly from 25 sampling-point measurements. Specifically, MAE and RMSE are reduced from the 10^{-2} level to the 10^{-4} level. PSNR increases from approximately 2.3 dB to 30.58 dB, 30.21 dB, and 28.3 dB, respectively. Meanwhile, R^2 increases from negative values to 0.983, 0.988, and 0.978, and SSIM improves from about 0.13 to 0.9998. For all three magnetic-field distributions, the five metrics consistently indicate high-fidelity image reconstruction.

Fig. 5 illustrates the influence of sampling number and sampling strategy, using the magnetic-field distribution with three extrema as an example. Fig. 5(a) shows the average MAE as a function of the number of sampling points, where each data point represents the mean over 20 independent MABE reconstructions with different sampling sets. For square numbers of sampling points, locations are generated by adding normally distributed random perturbations to uniformly spaced grid points, with the displacement magnitude bounded to 30% of the field-of-view size; any remaining sampling points are drawn uniformly at random over the full field of view. As shown in Fig. 5(a), 25 sampling points are sufficient to maintain MAE stably at the 10^{-4} level. Balancing acquisition time and reconstruction fidelity, we therefore identify 25 sampling points as a practical compromise.

Fig. 5(b) compares MAE obtained using five sampling strategies. The first strategy (“random”) draws sampling points uniformly at random across the field of view. The next three strategies generate points uniformly along spiral, square-loop, and serpentine trajectories, respectively, with additional uniformly distributed perturbations bounded to 30% of the field-of-view size. The final strategy (“grid”) applies bounded uniform perturbations to the center coordinates of a uniform grid, as described above. Fig. 5(c) provides a visual comparison of sampling locations and the corresponding reconstructed magnetic-field images. Among the five strategies, the grid-based strategy yields the best reconstruction performance and is therefore adopted as the default sampling scheme for the MABE method.

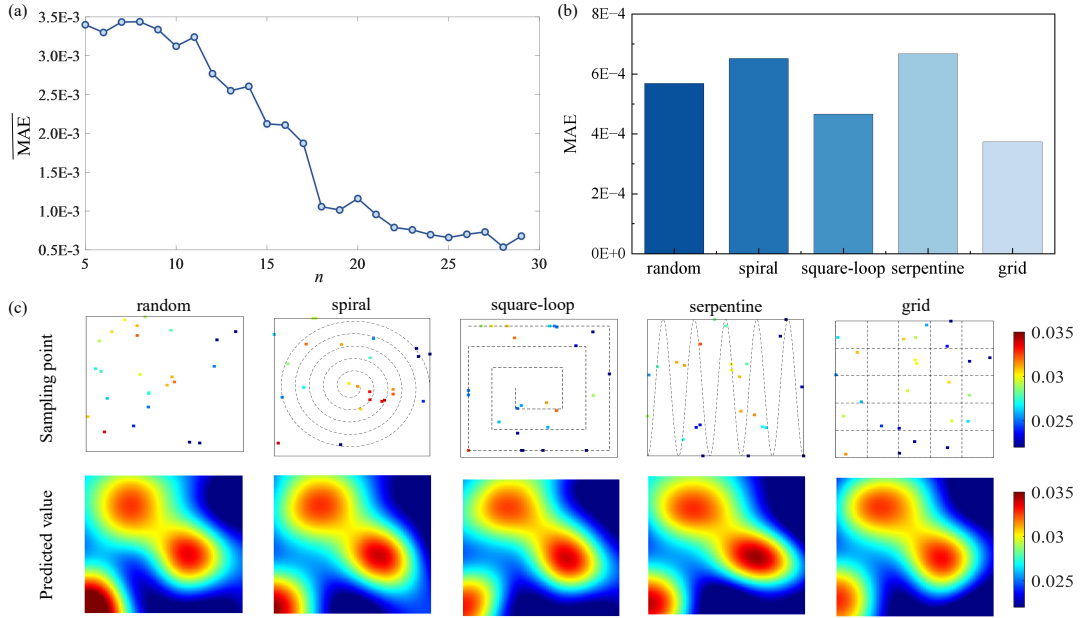


Figure 5: (a) Mean absolute error (MAE) over all 10^4 pixels of the reconstructed image as a function of the number of sampling points used in the MABE method. Each data point represents the average over 20 independent reconstructions. (b) MAE of reconstructed images obtained using MABE under five sampling strategies (see the main text). (c) Sampling-point locations for the five strategies and the corresponding reconstructed 10^4 -pixel images obtained using MABE.

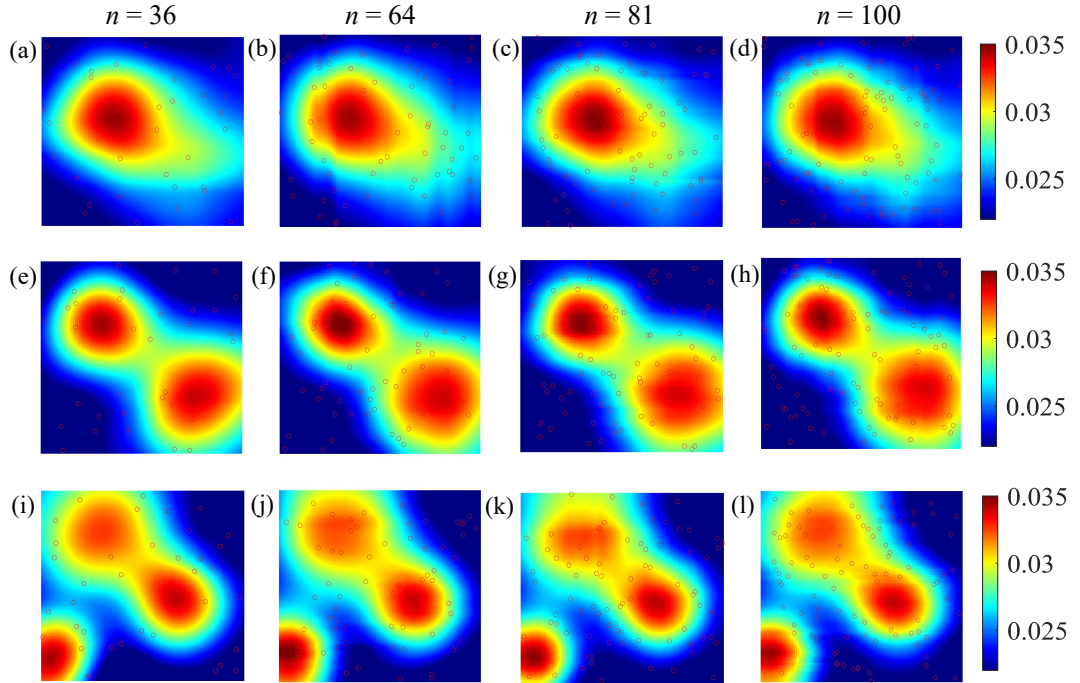


Figure 6: Reconstructed magnetic-field maps for distributions containing single, two, and three extrema using sampling numbers $n = 25, 36, 64, 81$, and 100 , respectively. The corresponding ground-truth magnetic-field distributions are shown in Fig. 2(a,e,i).

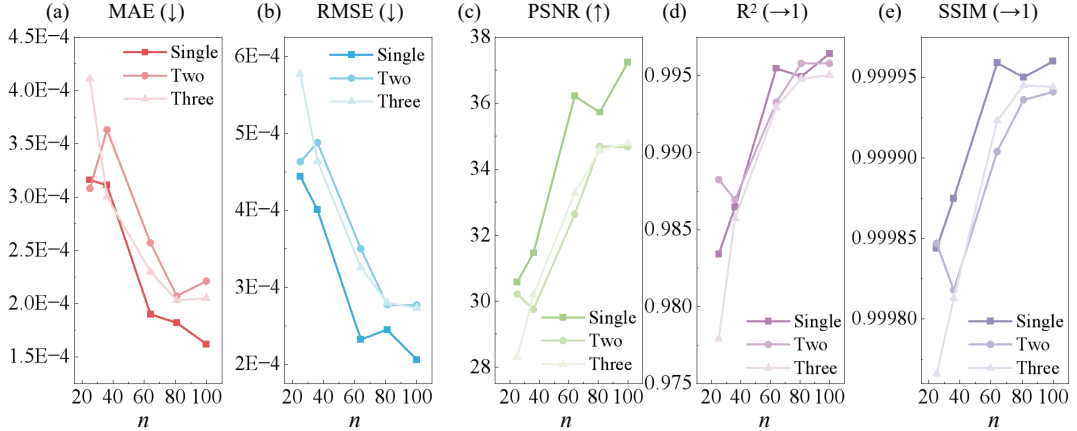


Figure 7: Quantitative image-quality metrics of the MABE reconstruction as the number of sampling points increases from 25 to 100: (a) mean absolute error (MAE); (b) root mean square error (RMSE); (c) coefficient of determination (R^2); (d) peak signal-to-noise ratio (PSNR); (e) structural similarity index (SSIM). Upward arrows in the titles indicate metrics for which larger values correspond to better performance, whereas downward arrows indicate metrics for which smaller values are better.

Fig. 6 and 7 show the reconstructed magnetic-field images and the corresponding quantitative metrics obtained using MABE as the sampling number increases from 25 to 36, 64, 81, and 100. With increasing sampling density, the reconstructed boundary features become progressively more consistent with the ground truth, and all evaluation metrics exhibit an overall improving trend. When 100 sampling points are used, SSIM exceeds 0.999 for all three distributions. Notably, although the number of sampling points increases by a factor of four from 25 to 100, the corresponding improvement in the quantitative metrics is relatively modest. In practical applications, the trade-off between sampling speed and reconstruction quality should therefore be carefully considered.

4 Discussion

In this work, we have introduced a training-free reconstruction framework enabling widefield NV magnetometry from a highly sparse set of sampling points. In representative simulations, magnetic-field images containing 10^4 pixels were successfully reconstructed from as few as 25 measurement points, achieving structural similarity index values exceeding 0.999. We further examined how sampling strategy and sampling density influence reconstruction performance. Compared with supervised learning-based approaches, the proposed method is training-free, structurally simple, and capable of maintaining good global prediction performance.

It should be emphasized that the high reconstruction fidelity observed at low sampling densities is primarily achieved for relatively smooth and structurally simple magnetic-field distributions. For more complex spatial patterns, reliable reconstruction is expected to require higher sampling densities or the incorporation of more sophisticated inference strategies. In particular, approaches inspired by compressed sensing and Gaussian-process-aided adaptive sampling [51, 52, 53, 54] may provide promising routes to incorporate stronger prior information and further enhance reconstruction quality.

In parallel, deep-learning-based reconstruction methods have demonstrated strong capability in restoring complex structures in medical imaging and super-resolution recovery of physical fields [55, 56, 57, 58, 59]. While many of these methods rely on large supervised training datasets, others—such as deep image prior approaches [57]—exploit implicit network priors without explicit training data. Although their applicability to quantitative NV magnetometry remains to be fully assessed, such methods offer intriguing possibilities for accelerating widefield imaging and addressing complex current distributions in integrated circuits and related systems.

Acknowledgments

The authors thank Yaxing Bian, Shuangping Han, Jiamin Li, Kai Song and Hongrui Liu for their valuable discussions and supports.

References

- [1] C. L. Degen, F. Reinhard, and P. Cappellaro. Quantum sensing. *Reviews of Modern Physics*, 89(3):035002, July 2017.
- [2] Marcus W. Doherty, Neil B. Manson, Paul Delaney, Fedor Jelezko, Jörg Wrachtrup, and Lloyd C. L. Hollenberg. The nitrogen-vacancy colour centre in diamond. *Physics Reports*, 528(1):1–45, July 2013.
- [3] Romana Schirhagl, Kevin Chang, Michael Loretz, and Christian L. Degen. Nitrogen-Vacancy Centers in Diamond: Nanoscale Sensors for Physics and Biology. *Annual Review of Physical Chemistry*, 65(1):83–105, 2014.
- [4] Dominik B. Bucher, Diana P. L. Aude Craik, Mikael P. Backlund, Matthew J. Turner, Oren Ben Dor, David R. Glenn, and Ronald L. Walsworth. Quantum diamond spectrometer for nanoscale NMR and ESR spectroscopy. *Nature Protocols*, 14(9):2707–2747, September 2019.
- [5] F. Dolde, H. Fedder, M. W. Doherty, T. Nöbauer, F. Rempp, G. Balasubramanian, T. Wolf, F. Reinhard, L. C. L. Hollenberg, F. Jelezko, and J. Wrachtrup. Electric-field sensing using single diamond spins. *Nature Physics*, 7(6):459–463, June 2011.
- [6] Nabeel Aslam, Matthias Pfender, Philipp Neumann, Rolf Reuter, Andrea Zappe, Felipe Fávaro De Oliveira, Andrej Denisenko, Hitoshi Sumiya, Shinobu Onoda, Junichi Isoya, and Jörg Wrachtrup. Nanoscale nuclear magnetic resonance with chemical resolution. *Science*, 357(6346):67–71, July 2017.
- [7] V. M. Acosta, E. Bauch, M. P. Ledbetter, A. Waxman, L.-S. Bouchard, and D. Budker. Temperature Dependence of the Nitrogen-Vacancy Magnetic Resonance in Diamond. *Physical Review Letters*, 104(7):070801, February 2010.
- [8] G. Kucsko, P. C. Maurer, N. Y. Yao, M. Kubo, H. J. Noh, P. K. Lo, H. Park, and M. D. Lukin. Nanometre-scale thermometry in a living cell. *Nature*, 500(7460):54–58, August 2013.
- [9] D. A. Broadway, B. C. Johnson, M. S. J. Barson, S. E. Lillie, N. Dontschuk, D. J. McCloskey, A. Tsai, T. Teraji, D. A. Simpson, A. Stacey, J. C. McCallum, J. E. Bradby, M. W. Doherty, L. C. L. Hollenberg, and J.-P. Tetienne. Microscopic Imaging of the Stress Tensor in Diamond Using in Situ Quantum Sensors. *Nano Letters*, 19(7):4543–4550, July 2019.
- [10] P. Kehayias, M. J. Turner, R. Trubko, J. M. Schloss, C. A. Hart, M. Wesson, D. R. Glenn, and R. L. Walsworth. Imaging crystal stress in diamond using ensembles of nitrogen-vacancy centers. *Physical Review B*, 100(17):174103, November 2019.
- [11] Francesco Casola, Toeno van der Sar, and Amir Yacoby. Probing condensed matter physics with magnetometry based on nitrogen-vacancy centres in diamond. *Nature Reviews Materials*, 3(1):17088, January 2018.
- [12] Edlyn V. Levine, Matthew J. Turner, Pauli Kehayias, Connor A. Hart, Nicholas Langellier, Raisa Trubko, David R. Glenn, Roger R. Fu, and Ronald L. Walsworth. Principles and techniques of the quantum diamond microscope. *Nanophotonics*, 8(11):1945–1973, November 2019.

- [13] Mason C. Marshall, Matthew J. Turner, Mark J. H. Ku, David F. Phillips, and Ronald L. Walsworth. Directional detection of dark matter with diamond. *QUANTUM SCIENCE AND TECHNOLOGY*, 6(024011), April 2021.
- [14] Matthew J. Turner, Nicholas Langellier, Rachel Bainbridge, Dan Walters, Srujan Meesala, Thomas M. Babinec, Pauli Kehayias, Amir Yacoby, Evelyn Hu, Marko Lončar, Ronald L. Walsworth, and Edlyn V. Levine. Magnetic Field Fingerprinting of Integrated-Circuit Activity with a Quantum Diamond Microscope. *Physical Review Applied*, 14(1):014097, July 2020.
- [15] James L. Webb, Luca Troise, Nikolaj W. Hansen, Louise F. Frellsen, Christian Osterkamp, Fedor Jelezko, Steffen Jankuhn, Jan Meijer, Kirstine Berg-Sørensen, Jean-François Perrier, Alexander Huck, and Ulrik Lund Andersen. High-Speed Wide-Field Imaging of Microcircuitry Using Nitrogen Vacancies in Diamond. *Physical Review Applied*, 17(6):064051, June 2022.
- [16] John F. Barry, Jennifer M. Schloss, Erik Bauch, Matthew J. Turner, Connor A. Hart, Linh M. Pham, and Ronald L. Walsworth. Sensitivity optimization for NV-diamond magnetometry. *Reviews of Modern Physics*, 92(1):015004, March 2020.
- [17] S. C. Scholten, A. J. Healey, I. O. Robertson, G. J. Abrahams, D. A. Broadway, and J.-P. Tetienne. Widefield quantum microscopy with nitrogen-vacancy centers in diamond: Strengths, limitations, and prospects. *Journal of Applied Physics*, 130(15):150902, October 2021.
- [18] Sungkun Hong, Michael S. Grinolds, Linh M. Pham, David Le Sage, Lan Luan, Ronald L. Walsworth, and Amir Yacoby. Nanoscale magnetometry with NV centers in diamond. *MRS Bulletin*, 38(2):155–161, February 2013.
- [19] Jared Rovny, Zhiyang Yuan, Mattias Fitzpatrick, Ahmed I. Abdalla, Laura Futamura, Carter Fox, Matthew Carl Cambria, Shimon Kolkowitz, and Nathalie P. de Leon. Nanoscale covariance magnetometry with diamond quantum sensors. *Science*, 378(6626):1301–1305, December 2022.
- [20] Paul Weinbrenner, Patricia Quellmalz, Christian Giese, Luis Flacke, Manuel Mueller, Matthias Althammer, Stephan Gepraegs, Rudolf Gross, and Friedemann Reinhard. Planar scanning probe microscopy enables vector magnetic field imaging at the nanoscale. *QUANTUM SCIENCE AND TECHNOLOGY*, 10(015037), January 2025.
- [21] Till Lenz, Arne Wickenbrock, Fedor Jelezko, Gopalakrishnan Balasubramanian, and Dmitry Budker. Magnetic sensing at zero field with a single nitrogen-vacancy center. *QUANTUM SCIENCE AND TECHNOLOGY*, 6(034006), July 2021.
- [22] Shashank Kumar, Pralekh Dubey, Sudhan Bhadade, Jemish Naliyapara, Jayita Saha, and Phani Peddibhotla. High-resolution spectroscopy of a single nitrogen-vacancy defect at zero magnetic field. *QUANTUM SCIENCE AND TECHNOLOGY*, 8(025011), April 2023.
- [23] J. Ebel, T. Joas, M. Schalk, P. Weinbrenner, A. Angerer, J. Majer, and F. Reinhard. Dispersive readout of room-temperature ensemble spin sensors. *QUANTUM SCIENCE AND TECHNOLOGY*, 6(03LT01), July 2021.
- [24] Kyu Young Han, Katrin I. Willig, Eva Rittweger, Fedor Jelezko, Christian Eggeling, and Stefan W. Hell. Three-Dimensional Stimulated Emission Depletion Microscopy of Nitrogen-Vacancy Centers in Diamond Using Continuous-Wave Light. *Nano Letters*, 9(9):3323–3329, September 2009.
- [25] Silvia Arroyo-Camejo, Marie-Pierre Adam, Mondher Besbes, Jean-Paul Hugonin, Vincent Jacques, Jean-Jacques Greffet, Jean-François Roch, Stefan W. Hell, and François Treussart. Stimulated Emission Depletion Microscopy Resolves Individual Nitrogen Vacancy Centers in Diamond Nanocrystals. *ACS Nano*, 7(12):10912–10919, December 2013.

- [26] Xiangdong Chen, Changling Zou, Zhaojun Gong, Chunhua Dong, Guangcan Guo, and Fangwen Sun. Subdiffraction optical manipulation of the charge state of nitrogen vacancy center in diamond. *Light: Science & Applications*, 4(1):e230–e230, January 2015.
- [27] Feng Xu, Jialong Chen, Yong Hou, Juan Cheng, Tony KC Hui, Shih-Chi Chen, and Zhiqin Chu. Super-Resolution Enabled Widefield Quantum Diamond Microscopy. *ACS Photonics*, 11(1):121–127, January 2024.
- [28] F. M. Stürner et al. Integrated and portable magnetometer based on nitrogen-vacancy centers. *Quantum Science and Technology*, 6(3):034011, 2021.
- [29] Fei Xie, Yuqiang Hu, Lingyun Li, Cao Wang, Qihui Liu, Nan Wang, Lihao Wang, Shuna Wang, Jiangong Cheng, Hao Chen, and Zhenyu Wu. A microfabricated fiber-integrated diamond magnetometer with ensemble nitrogen-vacancy centers. *Applied Physics Letters*, 120(19):191104, 2022.
- [30] Jonas Homrighausen, Frederik Hoffmann, Jens Pogorzelski, Peter Glösekötter, and Markus Gregor. Microscale fiber-integrated vector magnetometer with on-tip field biasing using NV ensembles in diamond microcrystals. *Physical Review Applied*, 22(3):034029, 2024.
- [31] Luca Basso, Pauli Kehayias, Jacob Henshaw, Gajadhar Joshi, Michael P. Lilly, Matthew B. Jordan, and Andrew M. Mounce. Wide-field microwave magnetic field imaging with nitrogen-vacancy centers in diamond. *Journal of Applied Physics*, 137(12):124401, 2025.
- [32] Mark J. H. Ku, Tony X. Zhou, Qing Li, Young J. Shin, Jing K. Shi, Claire Burch, Laurel E. Anderson, Andrew T. Pierce, Yonglong Xie, Assaf Hamo, et al. Imaging viscous flow of the dirac fluid in graphene. *Nature*, 583(7817):537–541, 2020.
- [33] Jiashen Tang, Zechuan Yin, Connor A. Hart, Jner Tzern Oon, Smriti Bhalerao, Jennifer M. Schloss, Matthew J. Turner, and Ronald L. Walsworth. Quantum diamond microscope for dynamic imaging of magnetic fields. *AVS Quantum Science*, 5(4):044403, 2023.
- [34] F. Jelezko and J. Wrachtrup. Single defect centres in diamond: A review. 203(13):3207–3225.
- [35] Genko T. Genov, Yachel Ben-Shalom, Fedor Jelezko, Alex Retzker, and Nir Bar-Gill. Efficient and robust signal sensing by sequences of adiabatic chirped pulses. 2(3):033216.
- [36] T. Ishikawa, A. Yoshizawa, Y. Mawatari, and others. Influence of dynamical decoupling sequences with finite-width pulses on quantum sensing for ac magnetometry. *Physical Review Applied*, 10(5):054059, 2018.
- [37] Tobias Nöbauer, Andreas Angerer, Björn Bartels, Michael Trupke, Stefan Rotter, Jörg Schmiedmayer, Florian Mintert, and Johannes Majer. Smooth optimal quantum control for robust solid-state spin magnetometry. *Phys. Rev. Lett.*, 115:190801, Nov 2015.
- [38] Ming Chen Wang and G. E. Uhlenbeck. On the theory of the brownian motion ii. *Rev. Mod. Phys.*, 17:323–342, Apr 1945.
- [39] Daniel T. Gillespie. Exact numerical simulation of the ornstein-uhlenbeck process and its integral. *Phys. Rev. E*, 54:2084–2091, Aug 1996.
- [40] Jiazhao Tian, Haibin Liu, Yu Liu, Pengcheng Yang, Ralf Betzholz, Ressa S. Said, Fedor Jelezko, and Jianming Cai. Quantum optimal control using phase-modulated driving fields. 102(4):043707.
- [41] Mark D. Bowdrey, Daniel K.L. Oi, Anthony J. Short, Konrad Banaszek, and Jonathan A. Jones. Fidelity of single qubit maps. *Physics Letters A*, 294(5):258–260, 2002.
- [42] Michael A Nielsen. A simple formula for the average gate fidelity of a quantum dynamical operation. *Physics Letters A*, 303(4):249–252, 2002.

- [43] L. M. Pham, N. Bar-Gill, C. Belthangady, and others. Enhanced solid-state multispin metrology using dynamical decoupling. *Physical Review B*, 86(4):045214, 2012.
- [44] J. Tian, R. S. Said, F. Jelezko, and others. Bayesian-based hybrid method for rapid optimization of nv center sensors. *Sensors*, 23(6):3244, 2023.
- [45] Sonja Kuhnt and David M. Steinberg. Design and analysis of computer experiments. *Statistical Science*, 4(4):409–423, 1989.
- [46] Donald R. Jones, Matthias Schonlau, and William J. Welch. Efficient global optimization of expensive black-box functions. 13(4):455–492.
- [47] J. Fox. *Applied Regression Analysis and Generalized Linear Models*. SAGE Publications, 2015.
- [48] Zhou Wang, A.C. Bovik, H.R. Sheikh, and E.P. Simoncelli. Image quality assessment: From error visibility to structural similarity. *IEEE Transactions on Image Processing*, 13(4):600–612, April 2004.
- [49] Rafael C. Gonzalez and Richard E. Woods. *Digital Image Processing*. Pearson, New York, fourth edition, global edition edition, 2017.
- [50] Tarald O. Kvålseth. Cautionary note about R 2. *The American Statistician*, 39(4):279–285, 1985.
- [51] Kyle P. Kelley, Maxim Ziatdinov, Liam Collins, Michael A. Susner, Rama K. Vasudevan, Nina Balke, Sergei V. Kalinin, and Stephen Jesse. Fast Scanning Probe Microscopy via Machine Learning: Non-Rectangular Scans with Compressed Sensing and Gaussian Process Optimization. *Small*, 16(37):2002878, September 2020.
- [52] Marti Checa, Addis S. Fuhr, Changhyo Sun, Rama Vasudevan, Maxim Ziatdinov, Ilia Ivanov, Seok Joon Yun, Kai Xiao, Alp Sehirlioglu, Yunseok Kim, Pankaj Sharma, Kyle P. Kelley, Neus Domingo, Stephen Jesse, and Liam Collins. High-speed mapping of surface charge dynamics using sparse scanning Kelvin probe force microscopy. *Nature Communications*, 14(1):7196, November 2023.
- [53] Chengfei Yang, Chaoyang Peng, Yuhang Chen, Tingting Luo, and Jiaru Chu. Space-filling scan paths and Gaussian process-aided adaptive sampling for efficient surface measurements. *Precision Engineering*, 54:412–419, October 2018.
- [54] Jiangshuai Li, Jiahao Zhou, Shaohui Yong, Yuanzhuo Liu, and Victor Khilkevich. Automatic sparse ESM scan using Gaussian process regression. In *2020 IEEE International Symposium on Electromagnetic Compatibility & Signal/Power Integrity (EMCSI)*, pages 671–675, Reno, NV, USA, July 2020. IEEE.
- [55] Chang Sun, Yitong Liu, and Hongwen Yang. Degradation-Aware Deep Learning Framework for Sparse-View CT Reconstruction. *Tomography*, 7(4):932–949, December 2021.
- [56] Chang Sun, Yazdan Salimi, Neroladaki Angeliki, Sana Boudabbous, and Habib Zaidi. An efficient dual-domain deep learning network for sparse-view CT reconstruction. *Computer Methods and Programs in Biomedicine*, 256:108376, November 2024.
- [57] Jia Wu, Jinzhao Lin, Xiaoming Jiang, Wei Zheng, Lisha Zhong, Yu Pang, Hongying Meng, and Zhangyong Li. Dual-Domain deep prior guided sparse-view CT reconstruction with multi-scale fusion attention. *Scientific Reports*, 15(1):16894, May 2025.
- [58] Thomas Braure, Delphine Lazaro, David Hateau, Vincent Brandon, and Kévin Ginsburger. Conditioning generative latent optimization for sparse-view computed tomography image reconstruction. *Journal of Medical Imaging*, 12(02), April 2025.

- [59] Adam M. Collins, Peter Rivera-Casillas, Sourav Dutta, Orie M. Cecil, Andrew C. Trautz, and Matthew W. Farthing. Super-resolution and uncertainty estimation from sparse sensors of dynamical physical systems. *Frontiers in Water*, 5:1137110, March 2023.